Journal of Theoretical and Applied Mechanics, Sofia, Vol.54 (2024) pp. 103-123
FLUID MECHANICS

EXPERIMENTS AND NUMERICAL MODELLING OF AIR-WATER FLOW IN UNSATURATED SOILS WITH HYSTERESIS AND AIR ENTRAPMENT

LONG NGUYEN TUAN[1]*, YVONNE LINS[2], EUGENIA STOIMENOVA[3], MARIA DATCHEVA[4], TOM SCHANZ[2]

[1]*F.A. Institute of Building Material Science, Bauhaus-Universität Weimar, Germany*
[2]*Former Chair of Foundation Engineering, Soil and Rock Mechanics, Ruhr-Universität Bochum, Germany*
[3]*Institute of Mathematics and Informatics, Bulgarian Academy of Sciences*
[4]*Institute of Mechanics and Institute of Information and Communication Technologies, Bulgarian Academy of Sciences*

[Received: 25 October 2022. Accepted: 9 March 2023]

doi: https://doi.org/10.55787/jtams.24.54.1.103

ABSTRACT: Air entrapment in soil-pores during cyclically hydraulic loading requires a physical insight by means of both modelling and experimental works. In the present study, transient drying and wetting tests are performed in a sand column device. The device enables to perform measurements of transient water content and pore water pressure in unsaturated soils. The measurements of water content as well as the pore pressure are directly linked to soil-water retention curve. The experimental results show that it exists an entrapped air together with hysteresis in soil water retention. Based on the experimental results, a new computer model of soil water retention is proposed. Finally, numerical simulation of air-water transport in unsaturated media is implemented using this model. The comparison between measured data and numerical simulation results shows that the proposed model can improve an accuracy in simulation of the water transport in unsaturated media.

KEY WORDS: air-water flow, entrapped air, hysteresis, modelling, soil water retention, unsaturated soil.

1 INTRODUCTION

Two-phase flow experiments are available for determining hydraulic properties of unsaturated soil. Experiments are performed either under steady-state or transient flow conditions. Transient state tests were reported in [1–3]. Commonly, this type

*Corresponding author e-mail: long.nguyen.tuan@uni-weimar.de

of tests are performed in a conventional column apparatuses. These apparatuses are equipped with sensors for measuring the capillary pressure–saturation relationship while drying and wetting the soil sample. However, these drying and wetting stages were not started from fully saturated condition with the result that the entrapped air in the soil and water retention curves (SWRC) was not clearly detected in these studies, although the phenomenon was recently discussed by [4, 5]. Furthermore, the sediment materials are formed generally by settling in the water e.g. river, sea. They are initially fully saturated until getting dried. In order to reproduce this initial state, we performed column type tests from initially fully water saturated condition in the column tests. Two drying and wetting cycles, which starting from initial fully saturated condition, were performed. During the testing procedure capillary pressure as well as water content were monitored by means of tensiometer and TDR sensors. The measured data allows tracking the transient capillary pressure and water content during drying and wetting cycles and to link capillary pressure and water content directly into SWRC. The experimental results show that there exists an entrapped air phenomenon together with hysteresis in soil water retention.

Regarding models of SWRC, several model concepts and formulations have been developed to simulate the hysteresis phenomenon measured. In general, models used to predict hysteretic SWRC can be classified into two categories: physically based models (e.g. domain models) and empirical models. Physical principle models based on the domain theory are introduced by several authors, e.g. by [6–8]. Other authors used empirical models for describing the hysteretic SWRC, [3, 9–12]. These models employ regression analysis to fit the experimental data.

However, each model has its advantages and disadvantages, which have been discussed in [13, 14]. While the domain theory model family [6, 8, 15] is complicated to implement in finite element (FE) code (see [9]), the scaling model family [3, 9, 11] has artificial pumping error (see [16]). The discussion of [16] showed that Mualem model [8] and Kool and Parker (KP) model [9] require storing a large number of soil moisture reversal points in the computer memory. From numerical simulation points of view, the SWR models should be parametrically controlled, simple and practical for implementing in FE code. Particularly, when the SWR model is coupled with the other laws such as flow law and stress-strain law, the computational convergence in numerical simulation must be stable.

Therefore, a new SWR model for sandy soils is proposed. The model is developed based on the basis of [17] and [18]. The main characteristics of the model is that air–entry and air–expulsion values vary depending on the state of saturation when transiting from wetting state to drying state and vice-versa. The model allows also to reproduce the entrapped air phenomenon which has been observed in the drying and wetting cycled experiments. The model does not require storing a large number

of soil moisture reversal points when simulates drying-wetting loops in FE method. Finally, the model is implemented incorporating with flow laws in a FE code. An agreement between numerical simulations and measurements shows that the SWR model can accurately predict water transport in unsaturated sandy soils.

2 Experiments of Transient SWRC and Results

The material used in the column tests was Hostun Sand [19] from France. Hostun Sand is a poorly graded medium-grained sand and according to USCS classification the sand is described as SP sand (ASTM D422-63).

A sand column testing device was used to conduct the transient state, where drainage and imbibition cycles were performed. During the transient state test, volume changes were measured by the attached dial gauge. The pore water pressure was measured by tensiometers (T1-T5) and the volumetric water content was determined using the readings of buriable-type TDR- sensors (TDR1-TDR5) see Fig. 1. Water was pumped in/out at the bottom of the column by an electronic pump. The device has been introduced in detail by [20].

A specimen with a height of about 540 [mm] and 300 [mm] in diameter was prepared by settling oven dry sand in the column filled with de-aired water, thus ensuring almost $100[\%]$ saturation. During the preparation procedure the water level was always kept above the sand specimen. Every ten centimeters, the void ratio in the column was checked using the accumulated mass of dry sand in the column. Following the experimental protocol, see Fig. 1 (right), the specimen was drained and wetted using the attached pump. Throughout the drainage process the water table was kept above the bottom water reservoir. The imbibition process was not stopped

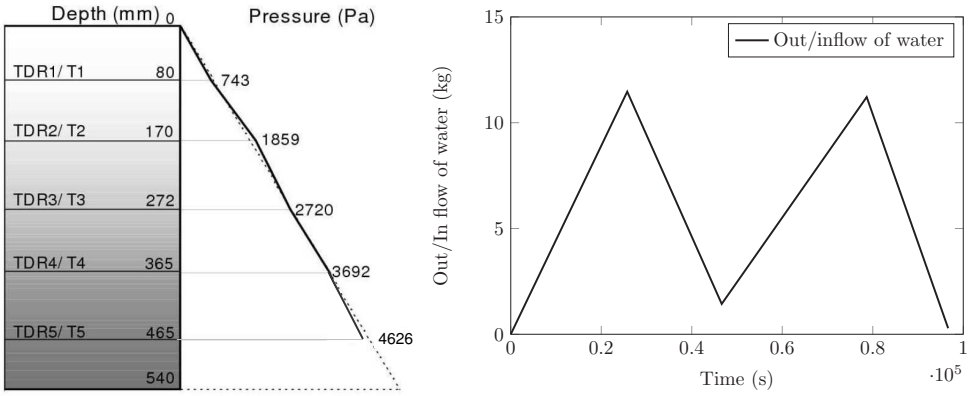

Fig. 1: (left) Initial conditions in the transient two-phase flow test and the depths of the sensors; (right) Water in/out flow by pumping from bottom.

until the water table reached the top of the sand specimen. Between each cycle the specimen was left for ≈ 12 hours to reach equilibrium state.

At the initial state, the measured pore water pressure increased with depth and almost exactly recover the gravimetric pressure, see Fig. 1. The measured degree of saturation at the beginning of the tests was equal or very close to 1 at each observation depth. The change of total volume of the column during the experiment is observed insignificant and therefore the degree of saturation may be considered proportional to the volumetric water content.

The water saturation obtained by means of the TDR sensors is plotted versus time in Fig. 2(left). Accordingly, the tensiometer measurements versus time are given in Fig. 2(right). The results from the first drying, the first wetting as well as of the second drying and second wetting cycles are shown in these figures.

As explained in Fig. 1 the sensor TDR 1 and the tensiometer T 1 are located at the top of the column and the sensor pair TDR 5 and T 5 is located at the bottom of the column. At the beginning of the wetting paths (first wetting path and second wetting path) the tensiometer T 1 measures lower negative pore-water pressure than tensiometer T 4, referring to a higher capillary pressure at the top of the sand specimen. The saturation at the top of the specimen is lower than the saturation at the bottom of the specimen. During wetting paths, the saturation increases corresponding to a decrease in capillary pressure, see Fig. 2(right). Saturated conditions are reached when the tensiometers measure positive pore-water pressure. During the wetting path the saturation increases first at the bottom of the specimen and then at the top of the specimen.

However, after the first wetting path the measurements obtained by TDR sensors and the observation on the column volume change show that the fully saturated con-

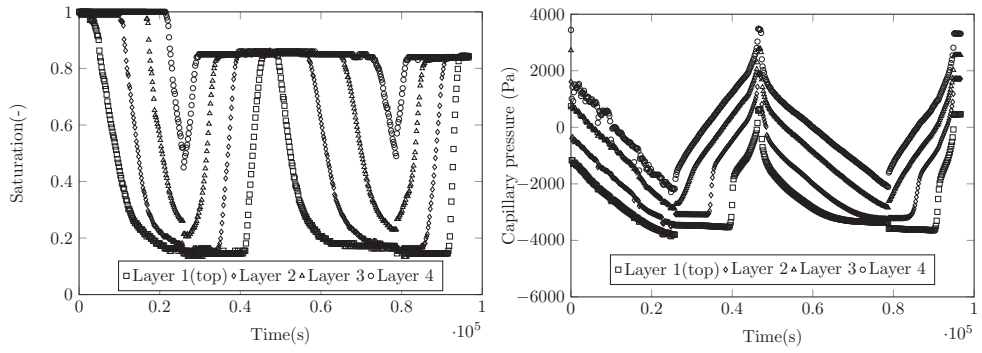

Fig. 2: (left) Results of TDR measurements; (right) results of tensiometer measurements.

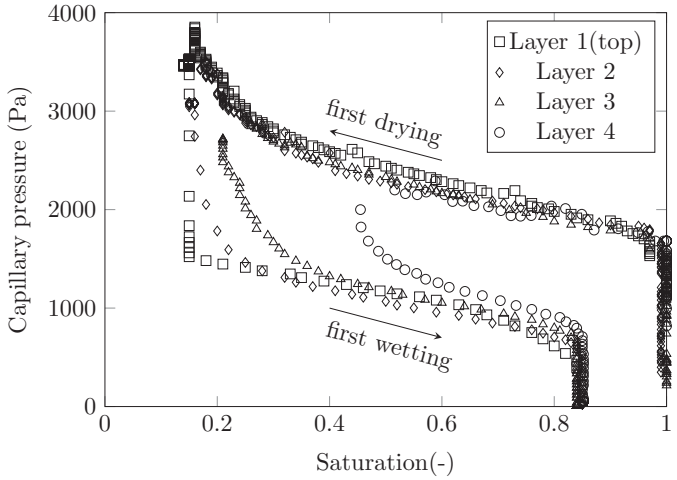

Fig. 3: Experimental results linked to the first drying and wetting cycle: TDR–sensors and tensiometer measurements.

dition is not recovered. This may be due to entrapment of air in soil pores that can not be removed by wetting process.

The readings of the tensiometers plotted against the corresponding TDR readings are given in Fig. 3. Only measured data of the first drying and wetting cycle measured at different depths are presented in the figure. TDR 5 and T 5 are always located in the saturated zone during the test and therefore the SWRC is plotted only for sensor pairs from TDR 1-T 1 to TDR 4-T 4.

The air-entry value, ψ_{aev}, is approximately 1600 [Pa]. After reaching this value, the saturation in the sand specimen decreases rapidly. The transition zone is between 1600 [Pa] to 3000 [Pa]. The residual zone starts at a relatively low capillary pressure in the drying cycle. The wetting paths result in different scanning curves, depending on the starting point for the wetting on the main drying curve. Due to the effect of air phase entrapped, the water saturation in wetting cycles reaches a maximum value, $S_l = 0.84$.

3 Modelling of the Hysteresis in SWRC

In this paper, two phenomenological models of hysteretic SWRC are introduced in order to reproduce the hysteresis phenomenon during drying-wetting cycle. The first model represents the hysteresis by means of two equations, one valid along the first drying path and another for the main wetting path. The scanning curves are modeled as linear lines, like a Hank model, connecting transition points between first drying

path and the main wetting path. The model has almost characteristics of the other previous models with drying curve, wetting curve, and scanning curve, but entrapped air phenomenon was not considered. We name it a former model. A second model, a new model, is an enhancement of the former model by the variation of air entry and air expulsion values during wetting-drying cycles. The entrapped air phenomenon is considered in the new model. The Hank model family was selected here to develop a new model, because it does not require Newton-Raphson method when implementing in finite element code at the beginning of the scanning curve. Therefore, the convergence of the problem is always guaranteed, even in a high frequency region of the drying-wetting loops.

In this section, we formulate the SWR model in the capillary pressure-saturation plane. We consider that the effective liquid saturation S_e is a scale of liquid saturation (S_l). Whilst S_l varies in their domain $[S_{lr}, S_{ls}]$, the S_e varied in a fixed domain [0,1]. The relation between S_l and S_e is defined as

$$S_e = \frac{S_l - S_{lr}}{S_{ls} - S_{lr}}\,, \tag{1}$$

where S_{ls} and S_{lr} are the maximum and the residual liquid degree of saturation, respectively. In the Mualem–van Genuchten SWRC model [18], S_e is related to the capillary pressure $\psi = P_g - P_l$ as follows

$$S_e = f\left(\psi, \lambda, P_0\right) = \left[1 + \left(\frac{\psi}{P_0}\right)^{\frac{1}{1-\lambda}}\right]^{-\lambda}\,, \tag{2}$$

where P_0 is a model parameter which represents the air entry value in soil drying path, λ is represents the shape of the slope. A function f has three variables: ψ, λ, P_0. In the original van Genuchten model, two variables λ and P_0 are considered the two parameters. Therefore, the model can not reproduce the hysteresis loops during soil wetting–drying cycles. In this study, the variables λ and P_0 are designed to change with conditions.

3.1 A FORMER HYSTERETIC SWR MODEL

For simulation of the hysteresis, the SWRC is defined through introducing equations for the first (or also for the main) drying curve and for the main wetting curve using the same functional form as in Fig. 2 but with different shape parameters, i.e. λ_d and $P_{0,d}$ for the first (or main) drying curve and λ_w and $P_{0,w}$ for the main wetting curve. The transition paths from main drying curve to main wetting curve (scanning or transition curves) are defined in this model as linear lines by the parameter dS_e. The schematic representation of the first model is shown in Fig. 4(a).

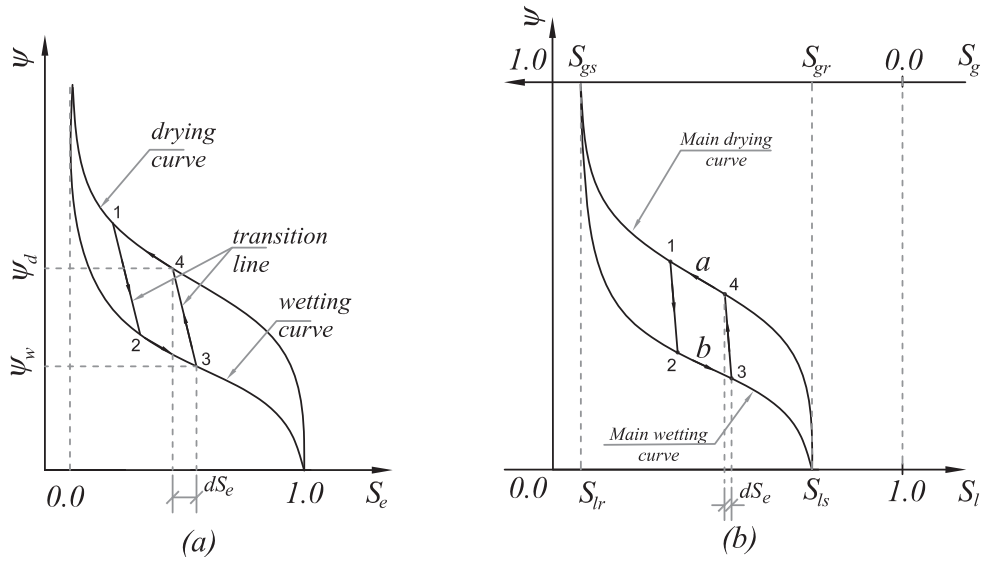

Fig. 4: Schematic representation of the former approach for modelling hysteresis in SWRC: (a) capillary pressure versus effective liquid saturation, (b) capillary pressure versus normal liquid saturation.

The state of water flow is changed via transition line. The particular transition line is determined by the value of the capillary pressure at which the transition loading path starts. The transition line is a straight parallel line to transfer from wetting state to drying state and vice-versa. The equation of the transition line is as follows:

$$S_e = \begin{cases} S_{e,w} - \dfrac{\psi - \psi_w}{\psi_d - \psi_w}\, dS_e & \text{for} \quad \text{wetting} \rightarrow \text{drying} \\ S_{e,d} + \dfrac{\psi_d - \psi}{\psi_d - \psi_w}\, dS_e & \text{for} \quad \text{drying} \rightarrow \text{wetting} \end{cases}, \tag{3}$$

where $S_{e,w}$ and $S_{e,d}$ are effective degree of saturation at beginning of transition state, ψ_d and ψ_w are transition points at drying curve and at wetting curve, respectively. Eq. 3 produces line 3-4 or line 1-2 in the Fig. 4. When the transition line meets the main wetting or main drying curve, it follows this curve according to:

$$S_e = \begin{cases} f(\psi|\lambda = \lambda_d, P_0 = P_{0,d}) & \text{for} \quad \text{drying path} \\ f(\psi|\lambda = \lambda_w, P_0 = P_{0,w}) & \text{for} \quad \text{wetting path} \end{cases}. \tag{4}$$

Equation 4 produces the curves 4-1 or 2-3 in the Fig. 4. The main drying curve and the main wetting curve meet each other when capillary pressure ψ is either equal to

zero or tends to infinity. The effective degree of saturation (S_e) is transformed to S_l by Fig. 1.

3.2 A NEW PROPOSED HYSTERETIC SWR MODEL

In the second model, a new parameter, a_{oc}, is introduced to account for the amount of the entrapped air during the initial drying path and the reduction of the maximum degree of saturation to $S_{oc} = S_{ls} - a_{oc}$. As soon as the degree of saturation drops below S_{oc} (see Fig. 5(b))it will not exceed this value again due to the entrapped air in the soil particles. By defining the effective saturation accordingly, this model will become equivalent to the previous one in the effective saturation–capillary pressure plane, Fig. 5(a). The equation for the effective degree of saturation is now as follows:

$$S_e = \frac{S_l - S_{lr}}{S_{ls} - S_{lr} - \langle S_{oc} - S_l \rangle a_{oc} / \left(S_{oc} - S_l\right)} , \tag{5}$$

where $\langle F \rangle = 0$ if $F < 0$ and $\langle F \rangle = F$ elsewhere. The Eq. 5 means that along the initial drying path S_e is defined by the Eq. 1. The Eq. 5 is launched when hydraulic loading deviates from the first drying path.

The model described in this section is developed within the previous modeling approach to the simulation of the drying-wetting hysteresis loops. The experimental

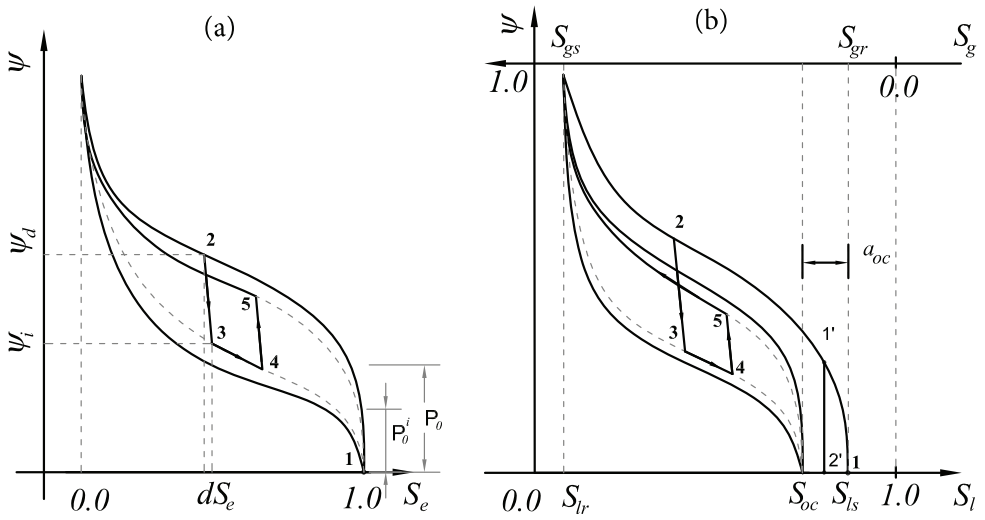

Fig. 5: Schematic representation of the proposed approach for modelling hysteresis in SWRC: (a) capillary pressure versus effective liquid saturation, (b) capillary pressure versus normal liquid saturation.

results of drying-wetting test reveal that the air–entry and the air–expulsion values are dependent on the current position in the capillary pressure–effective saturation plane. We propose a model that is able to reproduce both the reduction of the maximum saturation due to air entrapment and the variation of the air entry and the air expulsion with drying–wetting cycles. The SWRC parameter that represents the air entry ($P^j_{0,d}$) or the air expulsion ($P^j_{0,w}$) values is modified to depend on the development of the drying–wetting process. The proposed equations are:

$$P^j_{0,w} = P_{0,w} + \left(S^j_{e,d}\right)^n \left(P_{0,d} - P_{0,w}\right), \tag{6}$$

$$P^j_{0,d} = P_{0,d} + \left(1 - \left(S^j_{e,w}\right)^n\right) \left(P_{0,w} - P_{0,d}\right), \tag{7}$$

where, n is a model parameter which determines the magnitude of air-entry and expulsion values variation at the transition from drying to wetting, $S^j_{e,d}$ and $S^j_{e,w}$ are the effective saturation at transient positions of j^{th} drying-wetting loop. The equation of the transition line is written in Fig. 3. The scanning curves in the Fig. 4 are rewritten as

$$S_e = \begin{cases} f(\psi, P^j_{0,d} | \lambda = \lambda_d) & \text{for drying path} \\ f(\psi, P^j_{0,w} | \lambda = \lambda_w) & \text{for wetting path} \end{cases}. \tag{8}$$

The mathematical model of hysteretic SWRC is illustrated in Fig. 5. If at the initial state the liquid saturation S_l is less than S_{oc} the drying and wetting paths only go inside the domain drawn by the main drying and wetting curves b and c, respectively and the transient path follow e.g. line 4–5, see Fig. 5(b). If at the initial state S_l is in between S_{oc} and S_{ls}, there are two possibilities: (i) the soil state is at first drying path and for drying process, the drying goes along curve a until e.g. point 2, the scanning curve is in between points 2 and 3 and the wetting and dry cycle will follow the path $3 \rightarrow 4 \rightarrow 5$; ($ii$) for wetting process, the wetting path follows a scanning line up to capillary pressure equal to zero (line 1'-2') in Fig. 5(b).

3.3 Comparison with experimental data

In this subsection, the two models are verified with experimental data and with the other models. For illustrating all the characteristics of the new model, two types of SWR experiment are selected: the experiments which show entrapped air phenomenon and the experiments which show scanning curve at different transition points. For the early one, three types of soil are selected: Beaver Creek sand, Saskatchewan silt [21] and Hostun sand (this study). For the latter one, two types of soil are selected: a Robicon sandy loam [22] and a sand [23].

Table 1: Material parameters for SWRC

Parameter	P_{0d}	λ_d	S_{rl}	S_{ls}	P_{0w}	λ_w	a_{oc}	dS_e	n
Unit	kPa				kPa				
Huston sand	2.3	0.875	0.10	0.95	1.1	0.836	0.12	0.18	0.5
Beaver Creek sand	4.0	0.542	0.20	0.97	1.8	0.641	0.09	0.1	0.7
Saskatchewan silt	25	0.512	0.22	0.94	10	0.501	0.06	0.05	1.8
Sand	4.1	0.910	0.20	1.0	2.4	0.806	0.093	0.2	0.35
Sandy loam	10	0.754	0.32	1.0	2.2	0.486	0.1	0.01	1.6

The parameters of the new model are presented in Table 1. The model parameters S_{rl}, S_{ls}, a_{oc}, dS_e can be determined directly from experimental results. The parameters $P_{0,d}$, λ_d and $P_{0,w}$, λ_w, n are determined based on fitting considering the pore-size distribution suggested by [18]. It is proposed in [18] that soils having narrow pore-size distribution cause the steep of the soil-water retention slope, thus resulting in a large value of λ. Fine grain soils have air entry value P_0 and value n greater than coarse grain soils. There are no transition points in experimental data provided by [21], therefore the prediction curves start at initial saturated condition to residual saturated condition. The prediction curves in Fig. 6 include a main drying curve, a main wetting curve, and a secondary drying curve. The transition points in our model for Fig. 7a are $S_e = [0.3, 0.43, 0.57, 0.7]$ and for Fig. 7b are $S_e = [0.48, 0.62, 0.81]$. The prediction curves in Fig. 7 include a main drying curve, a main wetting curve, and scanning curves. When computing with the former model, the parameters of the new model (a_{oc} and n) are excluded.

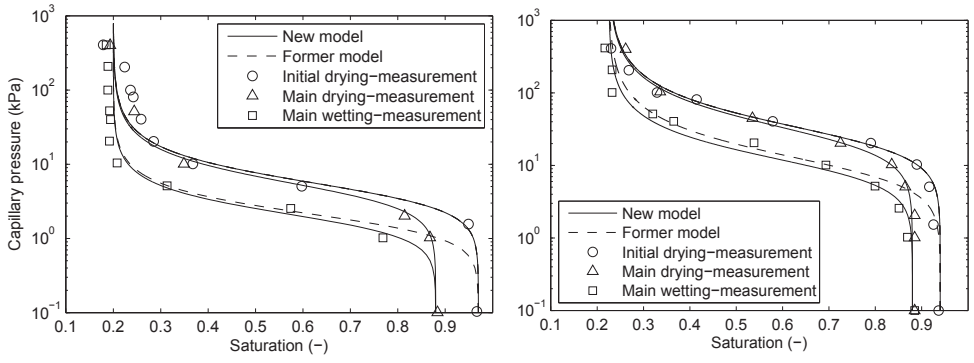

(a) Beaver Creek sand (b) Saskatchewan silt

Fig. 6: Comparison with laboratory measured data

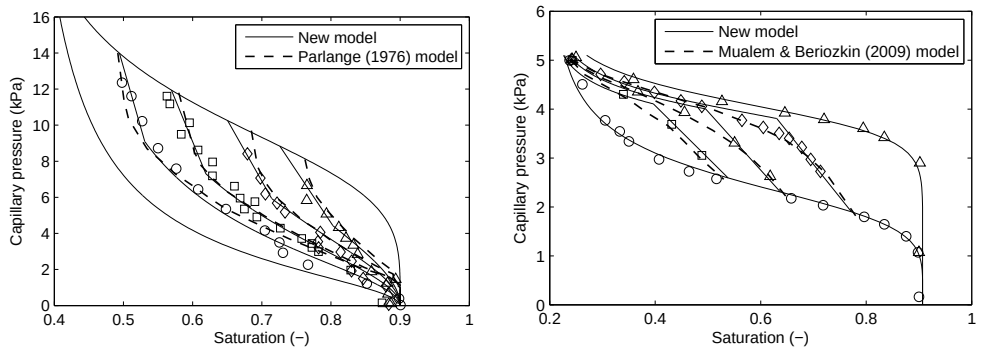

(a) Rubicon sandy loam (b) Sand

Fig. 7: Comparison with laboratory measured data – denoted by (□ △ ○ ◊)

Figure 6 presents the fitting curve between model and measured data given by [21]. According to [21], the volume change was considered negligible in their experiments. It is clear that when both soils are initially saturated, the initial drying curve of former model and new model are the identical. However, the wetting curves of the two models are different, because entrapped air is considered in the new model. Consequently, the maximum saturation of the main wetting curve modeled by new model is smaller than the initial maximum value. On the contrary, the main wetting curve and initial drying curve in the former model have the same maximum saturation value. Because of the difference from the initial value of main drying curves modelled by two models, the main drying curves of two models are different. In summary, the new model curve fits the experimental data better than the former model.

Figure 7 shows the comparison of the new model with the other models proposed by other authors. It is clear that a new simple model enables to reproduce the scanning curves similarly with the models proposed by [22] and by [24]. The measured data in Hostun sand test using axis translation experimental technique in this study is compared with the two models in Fig. 8. It is clear that the new model reproduces the different scanning curves based on the transition points in drying process or wetting process. Meanwhile, the former model, the scanning curve is constantly starting from initial drying curve to main wetting curve. The entrapped air phenomenon is not taken into account in the former model therefore it can not reproduces well the fitting with experimental data. The entrapped air phenomenon was also not taken into account in the SWR models proposed by the other authors, thus these models can also not fit well with measured data as compared with the new model.

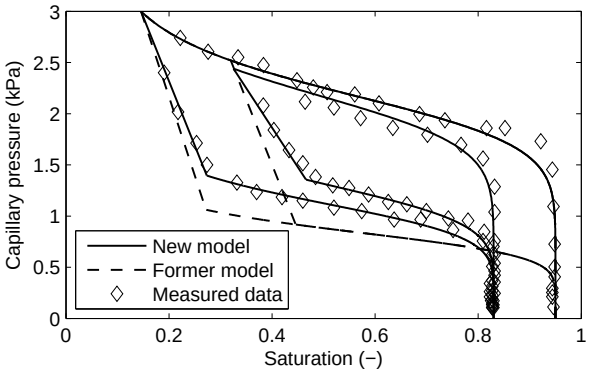

Fig. 8: Comparison of laboratory measured data for Hostun sand with soil model

4 NUMERICAL MODELLING OF TWO-PHASE FLOW

According to the experimental observation the sand column may be considered as non-deformable and therefore the equilibrium of mechanical forces is not considered. Equations for mass balance are established for gas and liquid phase. We assume that there are no gas dissolved in liquid phase and vice-versa.

4.1 MASS BALANCE OF WATER AND AIR

Mass balance equations for water ($\alpha = w$) and air ($\alpha = a$) in the pores are written as:

$$\frac{\partial}{\partial t}\left(\theta_\alpha S_\alpha \phi\right) + \nabla \cdot \boldsymbol{q}_\alpha = f_\alpha \ , \tag{9}$$

where, S_α is degree of saturation of liquid/gas phase, ϕ is porosity, θ_α is mass of liquid or gas per unit volume, $\boldsymbol{q}_\alpha$ is an advective fluxes of liquid/gas, and f_α denotes the external supply of phase. The dependent variable S_α has to be related to the unknowns e.g. our case P_l and P_g. The relation between degree of saturation S_l and liquid/gas pressures is established by SWR model. The relation between gas phase saturation and liquid phase saturation always obeys the following relation: $S_l + S_g = 1$.

4.2 CONSTITUTIVE EQUATIONS

The advective flow of the water phase described by the generalized Darcy's law and the equation for the advective flux $\boldsymbol{q}_\alpha$ is

$$\boldsymbol{q}_\alpha = -\frac{\boldsymbol{k} k_{r\alpha}}{\mu_\alpha}\left(\nabla P_\alpha - \rho_\alpha \boldsymbol{g}\right) \ , \tag{10}$$

where, μ_α is the dynamic viscosity of the phase α(gas/liquid), $\boldsymbol{g}$ is the gravity acceleration vector, ρ_α is the phase density, $\boldsymbol{k} = \text{diag}(k_{xx}, k_{yy}, k_{zz})$ is a tensor of intrinsic permeability, assuming that the material is isotropic,thus, one entry of the tensor can define the matrix $\boldsymbol{k}$, and finally, $k_{r\alpha}$ is the relative permeability of phase.

The liquid relative permeability k_{rl}, is derived from the Mualem–van Genuchten closed form model ([18]) for liquid phase:

$$k_{rl} = \sqrt{S_e}\left[1 - \left(1 - S_e^{1/\lambda}\right)^{\lambda}\right]^2, \tag{11}$$

where, λ is a SWRC shape parameter and S_e is an effective degree of saturation. The relative permeability k_{rg} for gas phase is follows:

$$k_r^g = 1 - k_{rl}. \tag{12}$$

The effective saturation (S_e) is computed based on the relation between capillary pressure and degree of saturation, which is presented as in Fig. 2 in the previous section.

4.3 Numerical approach

The two phase flow model is implemented by solving a system of balance equations. Constitutive equations are used to connect between primary unknowns (liquid pressure and gas pressure) to parameters and dependent variables like water saturation, water flux. The numerical analysis is composed by two terms: spatial and temporal discretization. The FE method is used to solve in spatial discretization in each time step. Because the problem presented here is temporally non-linear, the Newton-Raphson method is used to solve temporal discretization iteratively. The numerical approach is introduced here based on the formulations in [25, 26] and [27]. The simulations are implemented in the Code_bright FE code. The balance equation includes two terms: storage terms (S_α) and advective flow terms (q_α)

4.3.1 Approach for storage terms

Considering a constant porosity ϕ, the first term of Eq. 9, which relates to liquid saturation is transformed as:

$$\int_\Omega N_i \phi \theta_\alpha \frac{\partial(S_\alpha)}{\partial t} \mathrm{d}\Omega = \int_{e_1} N_i \phi \theta_\alpha \frac{\partial(S_\alpha)}{\partial t} \mathrm{d}\Omega + \cdots + \int_{e_m} N_i \phi \frac{\partial(\theta_\alpha S_\alpha)}{\partial t} \mathrm{d}\Omega, \tag{13}$$

where N_i is shape function in FE method. Using approximations for temporal finite difference at time step k, every integral can be written as, for example:

$$\int_{e_m} N_i \phi \frac{\partial(\theta_\alpha S_\alpha)}{\partial t} \mathrm{d}\Omega \approx \phi_{e_m}^k \left(\frac{(\theta_\alpha S_\alpha)_{i,e_m}^{k+1} - (\theta_\alpha S_\alpha)_{i,e_m}^{k}}{t^{k+1} - t^k}\right)_{e_m} \int_{e_m} N_i \mathrm{d}\Omega, \tag{14}$$

This approximation allows us to make the space integration independently from the physical variables. Consequently, computation of geometrical coefficients is necessary only once for a given finite element mesh. The integral of shape function over an element is equal to V_{e_m}/n_{e_m} for the case of linear shape functions.

4.3.2 Approach for advective flow terms

The weighted residual method is applied to the balance equation. After that the Green theorem is used to reduce the order of the derivatives and the divergence of flows is transformed into two terms. One of them is with gradient of the shape function. The Darcy's law can be written at node i as follows:

$$(15)\quad -\int_\Omega \nabla^t N_i \theta_\alpha \boldsymbol{q}_\alpha \mathrm{d}\Omega = \Big(\int_\Omega \nabla^t N_i \theta_\alpha \frac{\boldsymbol{k} k_{r\alpha}}{\mu_\alpha} \nabla N_j \mathrm{d}\Omega\Big)(P_\alpha)_j - \int_\Omega \nabla^t N_i \theta_\alpha \frac{\boldsymbol{k} k_{r\alpha}}{\mu_\alpha} \rho_\alpha \boldsymbol{g} \mathrm{d}\Omega\,,$$

where j denotes the summation over the element nodes, $(P_\alpha)_j$ is node-wise variable, where its values are defined by nodes and interpolation over nodes by means of shape functions.

For the node i the volume Ω over which the integral in Eq. 15 has to be performed in composition of the elements $e_1, e_2, ..., e_m$. The contribution of element e_m to the total lateral flux toward node i is approximated as:

$$(16)\quad \Big(\int_{e_m} \nabla^t N_i \theta_\alpha \frac{\boldsymbol{k} k_{r\alpha}}{\mu_\alpha} \nabla N_j \mathrm{d}\Omega\Big)(P_\alpha)_j \approx \theta_\alpha \frac{\boldsymbol{k}(k_{r\alpha})^{k+\varepsilon}_{e_m}}{\mu_\alpha} \Big(\int_{e_m} \nabla^t N_i \nabla N_j \mathrm{d}\Omega\Big)(P_\alpha)^{k+\theta}_j,$$

where two different intermediate points are used: $(t^{k+\theta})$ is used for pressure, and $(t^{k+\varepsilon})$ for the relative permeability. The integrals of products of shape function gradient are considered influence coefficients. They have to be computed for each element but only once for the given mesh points.

A similar approximation is applied for the gravity term in Eq. 15. The evaluation of density element-wise is convenient in order to balance correctly pressure gradients with gravity forces at element level.

4.3.3 Boundary condition for the model

The boundary conditions for balance equations are incorporated by means of simple addition of nodal flow rates. The mass flow rate of phase α is written as

$$(17)\quad q_\alpha = (\omega_\alpha)^0 q^0_\alpha + (\omega_\alpha)^0 \gamma_\alpha (P^0_\alpha - P_\alpha)\,,$$

where, the superscript $(\cdot)^0$ stands for the prescribed values, ω_α is the mass fraction of water in phase α, P_α is the pressure in phase α, q_α^0 is the prescribed mass flow for phase α, and γ_α is the leakage coefficient, which follows a boundary condition as the Cauchy type. In particular cases, where only the flow rate is applied, γ_α is defined to be equal to zero.

5 Numerical Simulations of Sand Column Experiment

5.1 Geometry, parameters, initial and boundary conditions

The FE-model with its geometry and discretization is presented in Fig. 9(a,b). The positions of nodes are defined corresponding to the TDR sensors and tensiometers locations along the sand column height. Nodes 60, 48, 36, 22, and 8 are corresponding positions to the locations of the TDR and tensiometer pairs enumerated from 1 to 5 (i.e. layer 1 to 5) instrumented within the sand column.

The space at the top of the sand column is used to stores water, if the inflow water exceeds the water storage capacity of the sand column. It is named a water-bearing space (WBS), see Fig. 9. The WBS exists in the model in order to avoid a rapid increase in water pressure when the sand material reaches a fully saturated state and consequently, this may cause a non-convergence of the Newton–Raphson integration procedure. The SWRC of the WBS obeys the van Genuchten type law with very small P_0 as compared to the parameter P_0 of sand. This way, the existing

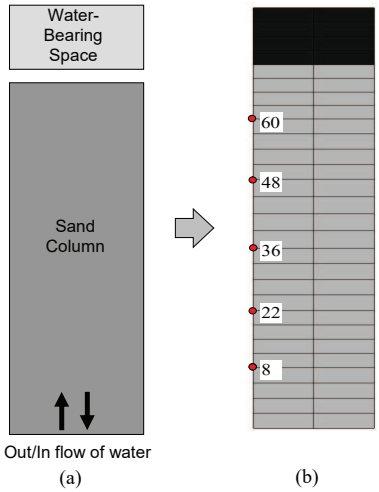

Fig. 9: Experimental description: (a) Materials and boundary conditions, (b) Geometry and discretization

Table 2: Material parameters

Unit	$P_{0,d}$ MPa	λ_d	S_{lr}	S_{ls}	$P_{0,w}$ MPa	dS_e	λ_w	$\boldsymbol{k}$	ϕ_0	n	a_{oc}
Sand	2.3E-03	0.875	0.12	1.0	6.0E-4	0.04	0.846	2.8E-11	0.47	0.25	0.16
WBS	5.0E-05	0.9	0.00	1.0	—	—	—	2.8E-07	0.98	—	—

of the WBS in the numerical model will not influence the wetting-drying process in sand material. No hysteresis and entrapped air phenomena are taken into account for WBS. The parameters of the materials are given in Table 2.

The liquid boundary conditions applied at the nodes at the bottom as prescribed liquid fluxes (q_α^0). The prescribed liquid flux values are presented in Fig. 1(right). At the initial state, the sand material is fully saturated and liquid pressure at the bottom boundary is prescribed to be equal to the gravimetric pore water pressure, that is P_l=5400 [Pa] at the bottom nodes. At the top, the gas pressure is applied on the nodes equal to atmosphere pressure ($P_g^0 = 100$ [Pa])

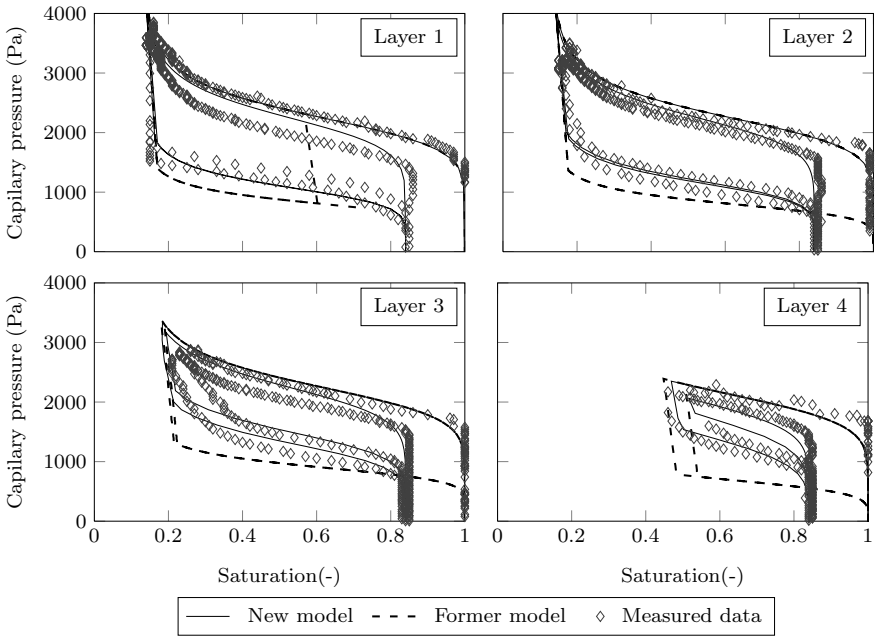

Fig. 10: Experiment vs. numerical simulation: capillary pressure and saturation.

5.2 Results and discussion

The results derived from numerical simulation are presented in time-dependence of the water saturation, the water pressure, and the capillary pressure. These results are compared with experimental results obtained in this study. The comparison of experimental and numerical SWRC results is given in Fig. 10, where capillary pressure is plotted against saturation. No entrapped air is taken into account in the former model. Therefore, the simulated saturation always reaches the value 1.0 after each drying-wetting loop. On the contrary, the entrapped air is considered by the parameter a_{oc}. Therefore, the maximum liquid saturation of the main drying and wetting curve is only equal to 0.84 (Fig. 10). Moreover, when the hydraulic loading starts from an ultimate state such as fully saturated or fully dry state, the wetting and drying curves in the numerical model are the same as the main wetting and drying curves in the experiment. But if the starting point of loading transition is not at an ultimate state, the soil water retention curves are located in between the main wetting and the main drying curves. The two wetting curves are not shown separately in the simulation at layer 1 (Fig. 10), because the transition points at the two wetting-drying loops are in close

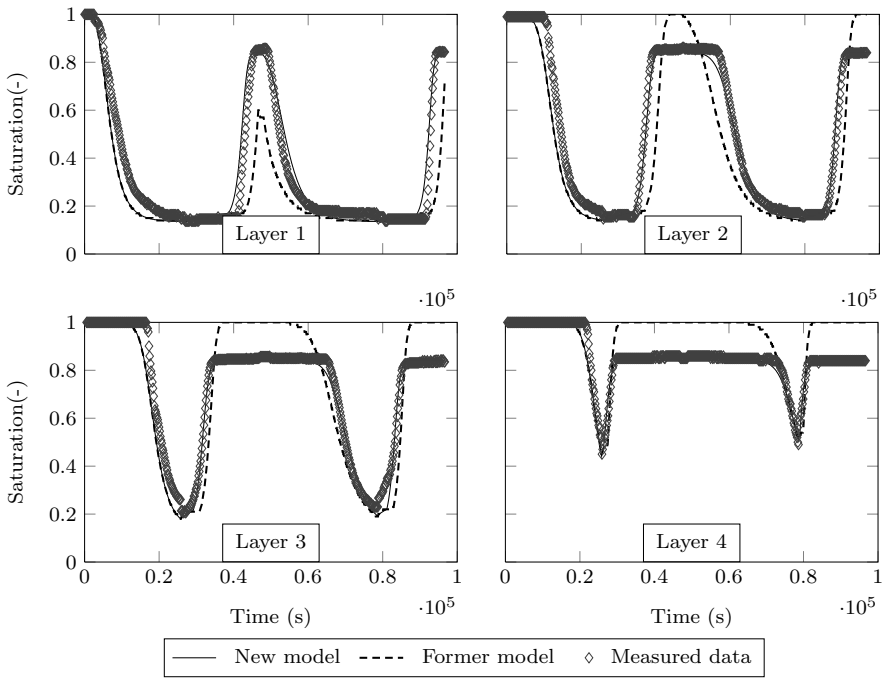

Fig. 11: Experiment vs. numerical simulation: degree of saturation and time.

proximity of each other. However, the difference between the first scanning wetting curve and the second scanning wetting curve in the numerical simulation can be seen clearly at layer 3 and layer 4. Overall, it can be seen that the new model can fit with experimental data better than the former model in terms of capillary pressure-suction relation.

Because the new SWR model considers the entrapped air, the maximum liquid saturation reaches after the first drying-wetting cycle also the value of 0.84. Consequently, the evolution of the liquid saturation obtained in the numerical simulation has a better agreement with the measured data (Fig. 11) when compared to the predictions of the simulation based on the former model. It it also can be seen from Fig. 11 (layer 1) that the first wetting curve can not reach to its maximum value by simulating with former model although the hydraulic boundary conditions are identical in the simulations with both models. It shows that the water/moisture transfer in unsaturated conditions faster when entrapped air is taken into account in SWR models.

Figure 12 presents the comparison between the measured and simulated capillary pressures versus time. It shows that the capillary pressure simulated by the new model

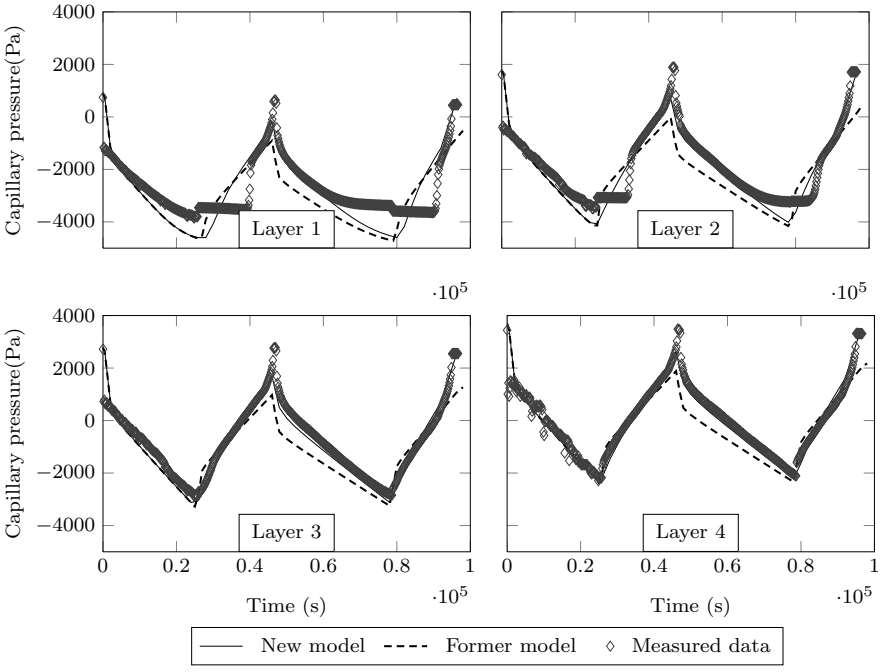

Fig. 12: Experiment vs. numerical simulation: liquid pressure and time.

results in a better agreement with measured data than the former model in layer 2, layer 3 and layer 4.

6 CONCLUSIONS

This paper presents experimental and numerical investigations of air-water flow considering the hysteresis and the entrapped air phenomena due to drying-wetting cycles in unsaturated sandy soils. A column testing device equipped with TDR and tensiometer sensors along the column height was used to monitor the water content and capillary pressure redistribution during wetting and drying loading paths. The experimental results evidence that there exists an entrapped air phenomenon together with hysteresis in soil water retention.

A new hysteretic water retention model is proposed. The model can reproduce aspects of the soil-air-water relation better than the other former models. Moreover, the model is simple to implement in a finite element code, thus its computational stability is guaranteed in coupling analysis with flow laws. The reduction of the maximum degree of saturation after the first drying path and the variation of the air-entry and air repulsion values with hydraulic loading cycles are special characteristics of this model. Numerical simulation of the experimental procedure is further presented in the paper in order to validate the effectiveness of the new model against former models in terms of unsaturated flow. The results derived from the numerical simulation of the column test based on the new model show a good agreement with the measured data. The study also shows that an improvement of SWR model enables to improve the simulation of water and air flows in porous media.

ACKNOWLEDGEMENTS

Maria Datcheva acknowledges the financial support by the Operational Programme Science and Education for Smart Growth (2014-2020) and the European Structural and Investment Fund through grant BG05M2OP001-1.001-0003. The work of Eugenia Stoimenova was financially supported by the National Science Fund of Bulgaria under Grant KP-06-N32/8.

REFERENCES

[1] G.C. TOPP, A. KLUTE, D.B. PETERS (1967) Comparison of water content-pressure head data obtained by equilibrium, steady-state and unsteady-state methods. *Soil Science Society of America, Proceedings* **31** 312-314.

[2] D. WILDENSCHILD, K.H. JENSEN, K.J. HOLLENBECK, T.H. ILLANGASEKARE, D. ZNIDARCIC, T. SONNENBORG, M.B. BUTTS (1997) A two-stage procedure for determining unsaturated hydraulic characteristics using a syringe pump and outflow observations. *Soil Science Society of America Journal* **61** 347-359.

[3] HAN CHEN HUANG, YI CHI TAN, CHEN WUING LIU, CHU HUI CHEN (2005) A novel hysteresis model in unsaturated soil. *Hydrological Processes* **19**(8) 1653-1665.

[4] E.C. LEONG, H. RAHARDJO (1997) Review of soil-water characteristic curve equations. *Journal of Geotechnical and Geoenvironmental Engineering* **123**(12) 1106-1117.

[5] N. LU, M. KAYA, B. COLLINS, J. GODT (2013) Hysteresis of unsaturated hydromechanical properties of a silty soil. *Journal of Geotechnical and Geoenvironmental Engineering* **139**(3) 507-510.

[6] D.H. EVERETT (1954) A general approach to hysteresis - part 3: a formal treatment of the independent domain model of hysteresis. *Transactions of the Faraday Society* **50** 1077-1096.

[7] G.C. TOPP (1971) Soil water hysteresis on silt loam and clay loam soils. *Water Resources Research* **7**(4) 914-920.

[8] Y. MUALEM (1976) A new model for predicting the hydraulic conductivity of unsaturated porous media. *Water Resources Research* **12** 593-622.

[9] J.B. KOOL, J.C. PARKER (1987) Development and evaluation of closed-form expressions for hysteretic soil hydraulic properties. *Water Resources Research* **23**(1) 105-114.

[10] X.S. LI (2005) Modelling of hysteresis response for arbitrary wetting/drying paths. *Computers and Geotechnics* **32**(2) 133-137.

[11] D. CANONE, S. FERRARIS, G. SANDER, R. HAVERKAMP (2008) Interpretation of water retention field measurements in relation to hysteresis phenomena. *Water Resources Research* **44** W00D12, 14pp.

[12] A. MAQSOUD, B. BUSSIRE, M. AUBERTIN, M. MBONIMPA (2012) Predicting hysteresis of the water retention curve from basic properties of granular soils. *Geotechnical and Geological Engineering* **30** 1147-1159.

[13] D.B. JAYNES (1984) Comparison of soil-water hysteresis models. *Journal of Hydrology* **75** 287-299.

[14] P. VIAENE, H. VEREECKEN, J. DIELS, J. FEYEN (1994) A statistical analysis of six hysteresis models for the moisture retention characteristic. *Soil Science* **157**(6) 345-355.

[15] Y. MUALEM (1984) A modified dependent-domain theory of hysteresis. *Soil Science* **137** 283-291.

[16] A.D. WERNER, D.A. LOCKINGTON (2007) Comment on "H.-C. Huang, Y.-C. Tan, C.-W. Liu and C.-H. Chen, A novel hysteresis model in unsaturated soil. Hydrological Processes 19 (2005)". *Hydrological Processes* **21**(3) 411-412.

[17] R.J. HANKS, A. KLUTE, E. BRESLER (1969) A numeric method for estimating infiltration, redistribution, drainage, and evaporation of water from soil. *Water Resources Research* **5**(5) 1064-1069.

[18] M.TH. VAN GENUCHTEN (1980) A closed-form equation for predicting the hydraulic conductivity of unsaturated soils. *Soil Science Society of America Journal* **44** 892-898.

[19] E. FLAVIGNY, J. DESRUES, B. PALAYER (1990) Note technique: Le sable d'Hostun RF. *Revue française de géotechnique* **53** 67-70.

[20] Y. LINS, T. SCHANZ, D.G. FREDLUND (2009) Modified pressure plate apparatus and column testing device for measuring SWCC of sand. *Geotechnical Testing Journal* **32**(5) 450-464.

[21] H.Q. PHAM, D.G. FREDLUND, S.L. BARBOUR (2003) A practical hysteresis model for the soil-water characteristic curve for soils with negligible volume change. *Géotechnique* **53**(2) 293-298.

[22] J.-Y. PARLANGE (1976) Capillary hysteresis and the relationship between drying and wetting curves. *Water Resources Research* **12**(2) 224-228.

[23] A. POULOVASSILIS, E.C. CHILDS (1971) The hysteresis of pore water:the non-independence of domains. *Soil Science* **112**(5) 301-312.

[24] Y. MUALEM, A. BERIOZKIN (2009) General scaling rules of the hysteretic water retention function based on Mualem's domain theory. *European Journal of Soil Science* **60**(4) 652-661.

[25] P.C.D. MILLY (1985) A mass-conservative procedure for time-stepping in models of unsaturated flow. *Advances in Water Resources* **8**(1) 32-36.

[26] M.B ALLEN III (1985) Numerical modelling of multiphase flow in porous media. *Advances in Water Resources* **8**(4) 162-187.

[27] S. OLIVELLA, J. CARRERA, A. GENS, E.E. ALONSO (1996) Numerical formulation for a simulator (CODE_BRIGHT) for the coupled analysis of saline media. *Engineering Computations* **13** 87-112.